DOI: 10.19884/j.1672-5220.202405002

A Hybrid Compensation Scheme for the Input Rate-Dependent Hysteresis of the Piezoelectric Ceramic Actuators

DONG Ruili[1*], TAN Yonghong[2*], HOU Jiajia[1], ZHENG Bangsheng[1]
1. College of Information Science and Technology, Donghua University, Shanghai 201620, China
2. College of Mechanical and Electronic Engineering, Shanghai Normal University, Shanghai 200234, China

Abstract: A hybrid compensation scheme for piezoelectric ceramic actuators (PEAs) is proposed. In the hybrid compensation scheme, the input rate-dependent hysteresis characteristics of the PEAs are compensated. The feedforward controller is a novel input rate-dependent neural network hysteresis inverse model, while the feedback controller is a proportion integration differentiation (PID) controller. In the proposed inverse model, an input rate-dependent auxiliary inverse operator (RAIO) and output of the hysteresis construct the expanded input space (EIS) of the inverse model which transforms the hysteresis inverse with multi-valued mapping into single-valued mapping, and the wiping-out, rate-dependent and continuous properties of the RAIO are analyzed in theories. Based on the EIS method, a hysteresis neural network inverse model, namely the dynamic back propagation neural network (DBPNN) model, is established. Moreover, a hybrid compensation scheme for the PEAs is designed to compensate for the hysteresis. Finally, the proposed method, the conventional PID controller and the hybrid controller with the modified input rate-dependent Prandtl-Ishlinskii (MRPI) model are all applied in the experimental platform. Experimental results show that the proposed method has obvious superiorities in the performance of the system.

Key words: hybrid control; input rate-dependent hysteresis; inverse model; neural network; piezoelectric ceramic actuator
CLC number: TP2 **Document code**: A
Article ID: 1672-5220(2024)04-0436-11

Open Science Identity (OSID)

0 Introduction

The piezoelectric ceramic actuators (PEAs) have been extensively applied in various fields such as biological science, aerospace, military and ultra-precision matching[1-4]. However, the hysteresis of the PEAs affects the positioning accuracy of the system and even causes the oscillation of the system, which makes the performances of the entire positioning platform degrade. Therefore, it is of great significance to study how to compensate or suppress hysteresis for the application of PEAs in micro-precision systems.

Many compensation schemes for hysteresis nonlinearities have been designed, which are mainly classified into three broad categories such as feedforward control based on the inverse model, model-free control and feedback control based on the inverse model.

In the feedforward control scheme, the hysteresis inverse model is established, and then it is used in the controlled system. For instance, the asymmetric Bouc-Wen inverse model[5] and the Krasnoselskii-Pokrovskii (KP) inverse model developed by inverse multiplicative structure[6] were considered as the feedforward controller to perform open-loop compensation for the hysteresis in the system. However, the major disadvantage of feedforward control is that its tracking performance is extremely sensitive to uncharted conditions such as immeasurable system noise and model errors. Aiming at resolving these problems, some robust compensators are designed[7]. Even so, the feedforward control scheme still has low suppression of uncertainties. Hence, model-free control schemes are extensively used in systems influenced by uncertainties. Raafat et al.[8] designed and analyzed the robust controller of the single-axis precision positioner, by considering the influences of uncertainties on the stabilities and performances of the system. Moreover, sliding mode controllers have also attracted more attention from domestic and foreign scholars. Liaw et al.[9] proposed an enhanced sliding mode controller, which could adapt to parameter uncertainties, nonlinearities and other uncertain disturbances. Although modeling methods based on the sliding mode concept had shown broad prospects for matching uncertainty, state estimation was still needed. On this basis, Peng et al.[10] proposed an observer based on the proportion integration differentiation (PID) sliding mode, but how to accurately estimate system parameters was a challenge. More than that, it is found that the

Received date: 2024-05-09
Foundation items: National Natural Science Foundation of China (Nos. 62171285, 61971120 and 62327807)
* Correspondence should be addressed to DONG Ruili, email: ruilidong@dhu.edu.cn; TAN Yonghong, email: Tany@shnu.edu.cn
Citation: DONG R L, TAN Y H, HOU J J, et al. A hybrid compensation scheme for the input rate-dependent hysteresis of the piezoelectric ceramic actuators[J]. *Journal of Donghua University (English Edition)*, 2024, 41(4): 436-446.

hysteresis in PEAs varies with the frequency of the input signal based on the experimental data, which is called the rate-dependent hysteresis (i.e., the dynamic hysteresis) in general. With the frequency f of the input signal increasing, the width of the hysteresis loop increases and the height decreases, as shown in Fig. 1.

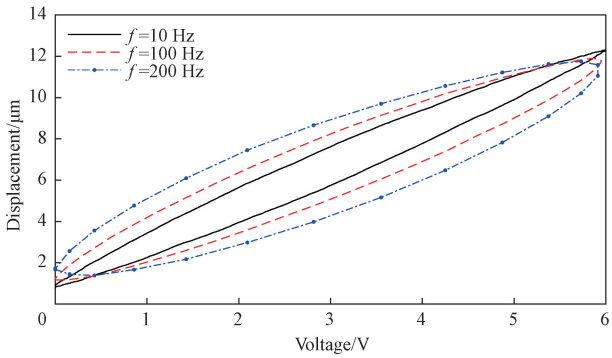

Fig. 1 Rate-dependent hysteresis input-output curves in PEAs

The model-free controller is often designed to provide high gain at low frequencies, but the gain provided is not sufficient at high frequencies. As the input signal frequency increases continuously, the tracking performances tends to deteriorate at high frequencies. Therefore, for the compensation of input rate-dependent hysteresis, the feedback control based on the inverse model was widely studied[11-13]. Chen et al.[13] proposed an adaptive inverse control compensation method in response to the limited accuracy of PEAs in broadband control, but the controller could not deal with the control of the system if the input frequency was higher than 50 Hz. Therefore, it is necessary to design an appropriate controller for the input rate-dependent hysteresis of PEAs.

Thus, a hybrid controller is designed for the input rate-dependent hysteresis of PEAs. The hybrid controller is composed of the feedforward controller and the PID controller, and the main innovation is the design of the feedforward controller. In the feedforward controller, the controller is a novel rate-dependent neural network hysteresis inverse model of PEAs. In the proposed inverse model, an input rate-dependent auxiliary inverse operator (RAIO) and output of hysteresis are constructed to expanded input space (EIS) which converts the hysteresis inverse with multi-value mapping to the hysteresis inverse single-value mapping, and based on the EIS method, the inverse model is built. The arrangement of the paper is listed as follows.

A hybrid controller is designed in Section 1. The input rate-dependent inverse model of the hysteresis-based neural networks as the feedforward sub-controller is built in Section 2, and in the inverse model, a novel RAIO is explored. After that, experimental results are presented in Section 3. Finally, the conclusions are presented in Section 4.

1 The Design of Hybrid Compensation Scheme

To compensate for the influences of input rate-dependent hysteresis in PEAs, a hybrid controller is designed. The structure of the proposed controller with a feedforward sub-controller and a feedback sub-controller is shown in Fig. 2.

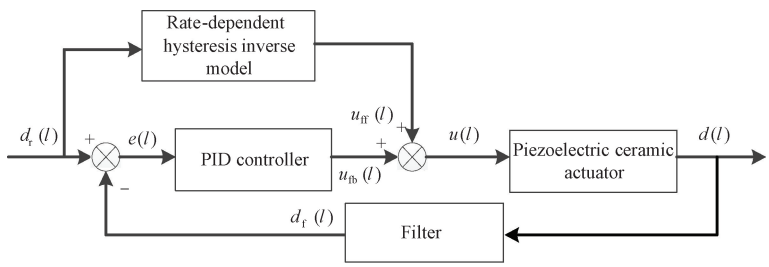

$d_r(l)$ — the reference; $u(l)$ — the output of the hybrid controller; l — the step of sample; $d(l)$ — the system output; $e(l)$ — the control error between the reference and the system output; $u_{fb}(l)$ — the output of the PID controller; $u_{ff}(l)$ — the output of the rate-dependent hysteresis inverse model; $d_f(l)$ — the output of the $d(l)$ after filter.

Fig. 2 Structure of control system

In Fig. 2, the controller is divided into two parts. One part is the proposed input rate-dependent hysteresis inverse model regarded as a feedforward sub-controller to compensate for input rate-dependent hysteresis of PEAs. The other part is the feedback PID controller, which is used to deal with model errors and unmeasurable noise in the control system. The PID controller is given by

$$u_{fb}(l) = K_p e(l) + K_i \sum_{j=0}^{l} e(l) + K_d[e(l) - e(l-1)], \quad (1)$$

where K_p, K_i and K_d are proportional, integral and differential gains, respectively.

Since the measurement noise of the sensor in the system will affect the control performance, a first-order low-pass filter illustrated in Eq. (2) is introduced to reduce the influence of noise on the stability of the system. The expression of the first-order low-pass filter in the system is

$$d_f(l) = \alpha d(l) + (1-\alpha) d_f(l-1), \quad (2)$$

where α is the coefficient of the filter; $d_f(l-1)$ is the output of the filter at the previous moment.

The feedforward sub-controller is a novel input rate-dependent hysteresis inverse model, and it will be presented in Section 2.

2 A Novel Input Rate-Dependent Hysteresis Inverse Model

2.1 Introduction of the inverse model

The inverse model determines the validation of the entire control system. There are usually two ways to obtain the inverse model: one is to directly identify the inverse model according to the input-output data, and the other is by solving the analytical inverse model by its corresponding positive model. Hysteresis is a multi-valued mapping, and it is not easy to obtain an inverse model from its corresponding hysteresis model[14-16]. Therefore, a rate-dependent inverse model is obtained by the direct identification method.

Similar to hysteresis properties, the hysteresis inverse shown in Fig. 3 has the characteristics of similar hysteresis, such as non-smoothness, rate-dependence and multi-valued mapping.

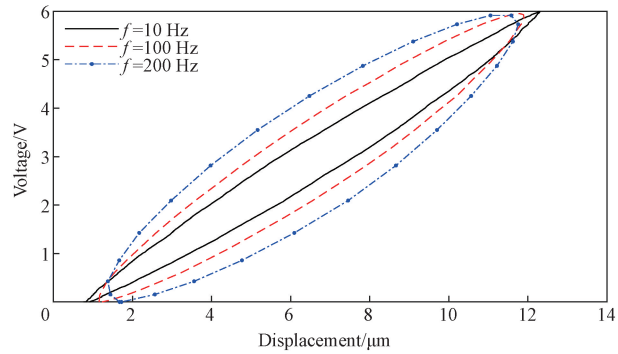

Fig. 3 Inverse hysteresis input-output curves in PEAs

Hence, an RAIO shown in Eq. (3) is proposed.

$$g(p(l),\ \Delta p(l)) = \begin{cases} e^{d_1(p(l)-p_e)} - e^{d_2|\Delta p(l)|}(p(l)-p_e) + g(p_e,\ 0) - 1, & \Delta p(l) \geqslant 0, \\ -e^{-d_1(p(l)-p_e)} - e^{d_2|\Delta p(l)|}(p(l)-p_e) + g(p_e,\ 0) + 1, & \Delta p(l) < 0, \end{cases} \tag{3}$$

where $p(l)$ represents the displacement of the PEAs, namely, the input of the inverse operator; $\Delta p(l) = p(l) - p(l-1)$ is the derivative of the system output, and it includes the information about the changing trend and frequency of the inverse model input; p_e is the dominant extreme value of the current system output; $g(p_e,\ 0)$ is the output of the RAIO at the local dominant extremum points; $d_1 > 0$ and $d_2 > 0$ are called the growth factor and the dilatation factor, respectively. The parameters d_1 and d_2 affect performances of the RAIO.

2.2 Influences of the growth factor and dilatation factor on the RAIO

2.2.1 Influence of the growth factor

In the case that $d_2 = 0.0002$, Fig. 4 provides the input-output curves of the RAIO when the growth factor d_1 changes. From Fig. 4, it can be seen that performances of $g(p(l),\ \Delta p(l))$ change rapidly as the growth factor d_1 changes, and the width of the input-output curve of the RAIO is different if the growth factor d_1 is different.

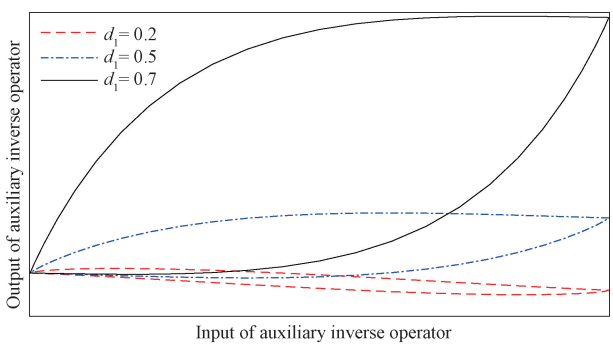

Fig. 4 Influence of growth factor d_1

2.2.2 Influence of the dilatation factor

Similarly, the input-output curves of the RAIO are provided in Fig. 5 (the dilatation factor d_2 changes but the growth factor d_1 keeps as 1). The width differences of the input-output curves of the RAIO in Fig. 5 are smaller than those in Fig. 4.

From Figs. 4 and 5, performances of the RAIO are in connection with d_1 and d_2.

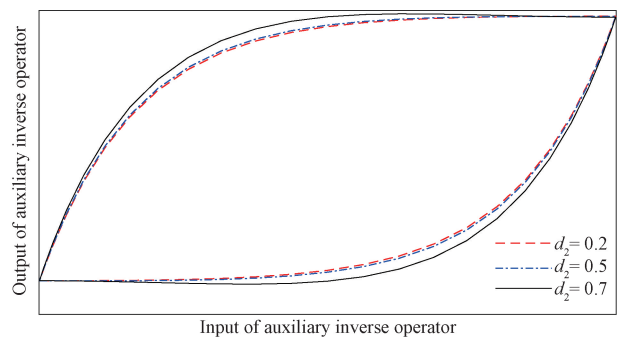

Fig. 5 Influence of growth factor d_2

2.3 Properties of the RAIO

The RAIO has the wiping-out property, rate-dependent property and continuity listed as follows.

2.3.1 Wiping-out property

In the process of increasing (decreasing) the excitation signal, when the point is larger (smaller) than the adjacent local maximum (minimum), the adjacent local maximum (minimum) is wiped out from the dominant extreme. In the RAIO, d_1 and d_2 are set to 0.7 and 1, respectively. The inverse operator is excited by the input signal shown in Fig. 6. The input-output of the RAIO is presented in Fig. 7.

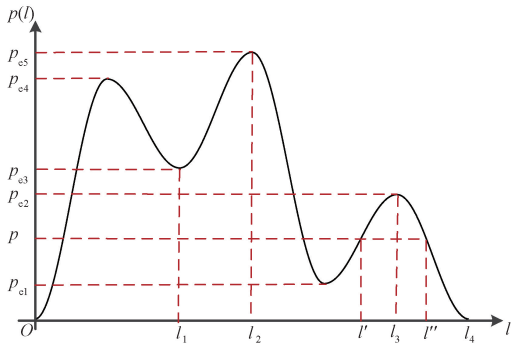

Fig. 6 Input signal of RAIO

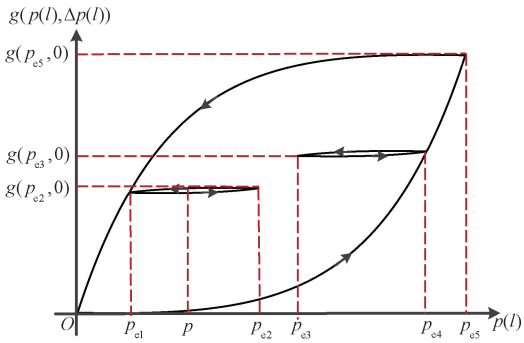

Fig. 7 Input-output of RAIO

For $l \in (l_1, l_2]$, when $p(l) \leqslant p_{e4}$, the current dominant extremum point is $(p_{e3}, g(p_{e3}, 0))$, but when $p(l) > p_{e4}$, the current dominant extremum point changes from $(p_{e3}, g(p_{e3}, 0))$ to $(0, 0)$, and the former dominant extremum point $(p_{e3}, g(p_{e3}, 0))$ is removed. Similarly, for $l \in (l_3, l_4]$, when $p(l) < p_{e1}$, the current dominant extremum changes from $(p_{e2}, g(p_{e2}, 0))$ to $(p_{e5}, g(p_{e5}, 0))$, and $(p_{e2}, g(p_{e2}, 0))$ is removed. From Fig. 7, the wiping-out property[17] of the auxiliary inverse operator is confirmed.

2.3.2 Rate-dependent property

The change in input frequency has a relationship with the derivative of the input[18]. Thus, an exponential term containing the input derivative is introduced into the proposed inverse operator. Figure 8 shows the input-output curves of the RAIO under the excitation of sinusoidal input with different frequencies. From Figs. 3 and 8, the width of the hysteresis loop generated by the RAIO increases with the increase of the input frequency, which is similar to the hysteresis system.

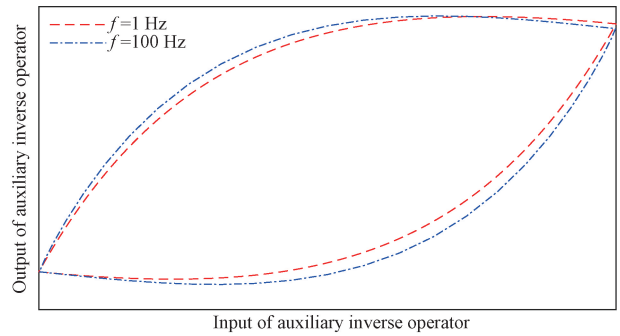

Fig. 8 Input-output of inverse operator under excitation of different frequency inputs

2.3.3 Continuity

Lemma 1 The output of the RAIO $g(p(l), \Delta p(l))$ is continuous with $p(l)$.

The proof of Lemma 1 is illustrated in Appendix A.

The neural network cannot be applied on mapping with multi-value directly. Based on the RAIO, the EIS method is employed to convert the multi-valued mapping to a one-to-one mapping, and the input rate-dependent neural network inverse model for hysteresis is built.

Lemma 2 Assume the input $p(l) \in C^2$, which is a smooth and continuous bounded function, there are two sampling times l', l'', where $l' \neq l''$, but $p(l') = p(l'') = p$. If $p(l')$ and $p(l'')$ are not extreme points, then $g(p(l'), \Delta p(l')) \neq g(p(l''), \Delta p(l''))$.

The proof of Lemma 2 is presented in Appendix B.

Theorem 1 For the presented inverse of the input rate-dependent hysteresis in PEAs, supposing that the input is given by Lemma 2, there will exist a continuous one-to-one mapping $E: \mathbf{R}^2 \rightarrow \mathbf{R}$. We can deduce that $\varphi(p(l)) = E(p(l), g(p(l), \Delta p(l)))$, where $\varphi(p(l))$ is the output of the neural networks model.

The proof of Theorem 1 is provided in Appendix C.

Based on the EIS method, a dynamic back propagation neural network (DBPNN) is implemented to characterize input rate-dependent hysteresis in PEAs. The structure of the system identification offline is explained in Fig. 9.

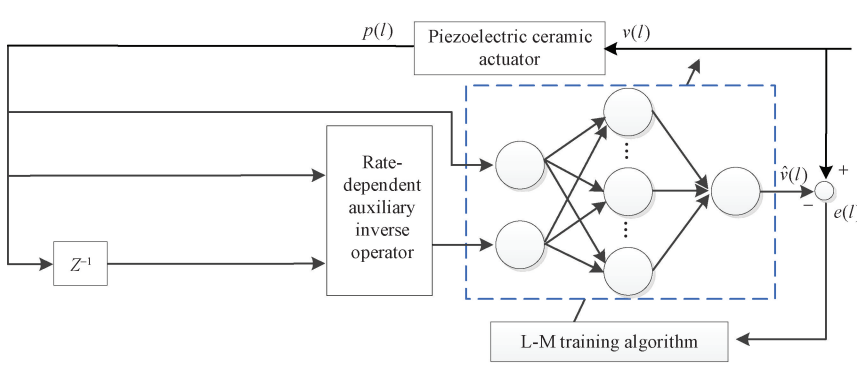

L-M training algorithm —Levenberg-Marquardt training algorithm.

Fig. 9 Structure of system identification

The cost function is defined as

$$E = \frac{1}{N}\sum_{l=1}^{N}(v(l) - \hat{v}(l))^2 = \frac{1}{N}\sum_{l=1}^{N}e(l)^2, \quad (4)$$

where N is the amount of data; $v(l)$ is the input of the PEAs; $\hat{v}(l)$ is the output of the inverse model.

$$\hat{v}(l) = h(\hat{\boldsymbol{W}}_3\,\sigma(\hat{\boldsymbol{W}}^{\mathrm{T}}\boldsymbol{P}(l) + \hat{\boldsymbol{B}}\mathrm{T}_1) + \hat{b}_2), \quad (5)$$

where $\boldsymbol{P}(l) = \begin{bmatrix} p(l) \\ g(p(l),\ \Delta\mathrm{p}(1)) \end{bmatrix}$ is the input space of the inverse model; $p(l)$ represents the displacement of the PEAs; $g(p(l),\ \Delta p(l))$ denotes the output of auxiliary inverse operator; $\hat{\boldsymbol{W}} = \begin{bmatrix} \hat{\boldsymbol{W}}_1 \\ \hat{\boldsymbol{W}}_2 \end{bmatrix} = \begin{bmatrix} \hat{w}_{11} & \hat{w}_{12} & \cdots & \hat{w}_{1m} \\ \hat{w}_{21} & \hat{w}_{22} & \cdots & \hat{w}_{2m} \end{bmatrix}$ and $\hat{\boldsymbol{W}}_3 = \begin{bmatrix} \hat{w}_{31} & \hat{w}_{32} & \cdots & \hat{w}_{3m} \end{bmatrix}$ are the weight space between the input-hidden layer and the hidden-output layer, respectively; $\hat{\boldsymbol{B}}_1 = \begin{bmatrix} \hat{b}_{11} & \hat{b}_{12} & \cdots & \hat{b}_{1m} \end{bmatrix}$ and $\hat{b}_2$ are the thresholds of the hidden layer and the output layer, respectively; $\sigma(\cdot)$ and $h(\cdot)$ are the sigmoid activation function and the linear activation function, respectively; m is set to the number of hidden layer neurons.

To facilitate the writing of the matrix, let $\hat{\boldsymbol{C}} = \begin{bmatrix} \hat{\boldsymbol{W}}_1 & \hat{\boldsymbol{W}}_2 & \hat{\boldsymbol{W}}_3 & \hat{\boldsymbol{B}}_1 & \hat{b}_2 \end{bmatrix} = \begin{bmatrix} \hat{c}_1 & \hat{c}_2 & \cdots & \hat{c}_{4m} & \hat{c}_{4m+1} \end{bmatrix}$. In addition, the L-M algorithm[19-20] is selected as a training algorithm because its rate of convergence is significantly quick. The corresponding Jacobian matrix $\boldsymbol{J}(c)$ can be obtained from

$$\boldsymbol{J}(c) = \begin{bmatrix} \dfrac{\partial e_1(c)}{\partial c_1} & \dfrac{\partial e_1(c)}{\partial c_2} & \cdots & \dfrac{\partial e_1(c)}{\partial c_{4m}} & \dfrac{\partial e_1(c)}{\partial c_{4m+1}} \\ \dfrac{\partial e_2(c)}{\partial c_1} & \dfrac{\partial e_2(c)}{\partial c_2} & \cdots & \dfrac{\partial e_2(c)}{\partial c_{4m}} & \dfrac{\partial e_2(c)}{\partial c_{4m+1}} \\ \vdots & \vdots & & \vdots & \vdots \\ \dfrac{\partial e_N(c)}{\partial c_1} & \dfrac{\partial e_N(c)}{\partial c_2} & \cdots & \dfrac{\partial e_N(c)}{\partial c_{4m}} & \dfrac{\partial e_N(c)}{\partial c_{4m+1}} \end{bmatrix}. \quad (6)$$

The iterative update formula of the L-M algorithm is as follows:

$$\hat{\boldsymbol{C}}^{(\lambda+1)} = \hat{\boldsymbol{C}}(\lambda) - [\boldsymbol{J}^{\mathrm{T}}\boldsymbol{J} + \mu\boldsymbol{I}]^{-1}\boldsymbol{J}^{\mathrm{T}}\mathrm{e}, \quad (7)$$

$$\mu = \begin{cases} 0.1\,\mu, & E^{(\lambda+1)} \leqslant E^{(\lambda)}, \\ 10\,\mu, & E^{(\lambda+1)} > E^{(\lambda)}, \end{cases} \quad (8)$$

where λ is the number of iterations.

A more detailed L-M training algorithm is illustrated below.

Step 1 Set the minimum value of the mean square error $\varepsilon > 0$ and the maximum number of iterations $\gamma = 150$. Let $\lambda = 1$, $\mu = 0.001$ and randomly initialize weights and biases.

Step 2 Calculate $E^{(\lambda)}$ according to Eq. (4), and then judge whether $E^{(\lambda)} < \varepsilon$. If $E^{(\lambda)} < \varepsilon$ or $\lambda > \gamma$, go to Step 5, otherwise go to Step 3.

Step 3 Calculate the Jacobian matrix $\boldsymbol{J}$ according to Eq. (6).

Step 4 Increase the number of iterations, and calculate updated parameter values $\boldsymbol{C}^{(\lambda+1)}$ on the basis of Eq. (7). Then calculate $E^{(\lambda+1)}$. If $E^{(\lambda+1)} \leqslant E^{(\lambda)}$, $\mu = 0.1\mu$, $\lambda = \lambda + 1$, else $\mu = 10\mu$, $\lambda = \lambda + 1$. Then, go to Step 2.

Step 5 Exit the loop.

In this paper, a DBPNN inverse model (abbreviated as DBPNN model) $NN(\cdot)$ satisfies

$$|\varphi(p(l)) - NN(p(l),\ g(p(l),\ \Delta p(l)))| \leqslant \xi,$$

where $\xi \geqslant 0$ is a bounded number indicating the model error.

Thus, the rate-dependent hysteresis inverse model in Fig. 2 can be written as

$$u_{\mathrm{ff}}(l) = NN(d_{\mathrm{r}}(l),\ g(d_{\mathrm{r}}(l),\ \Delta d_{\mathrm{r}}(l))).$$

Namely, a feedforward sub-controller is designed.

3 Experimental Results

The experimental platform is shown in Fig. 10. The PEAs (PZTS001) are driven by a voltage source. The maximum output displacement of the PEAs is (17.4±2.0) μm. The sampling frequency is 5 kHz. A piezoresistive displacement sensor is employed to measure the displacement of the actuator, and the input and the output data are collected by the card PCI-1716.

The proposed rate-dependent inverse hysteresis model and the designed controller are both used in the platform (Fig. 10). In the experiment, d_1 and d_2 in the model are selected as 0.12 and 0.18, respectively.

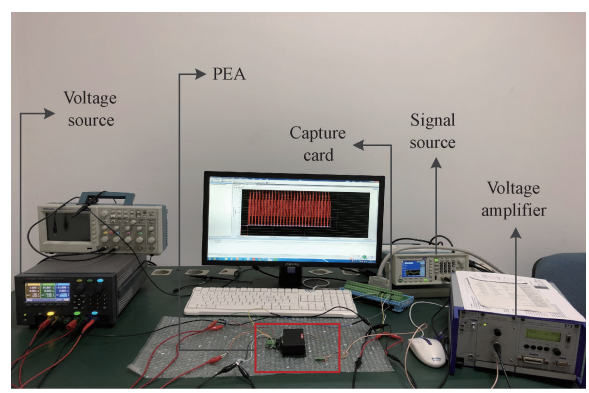

Fig. 10 Experimental platform

3.1 Validation of the DBPNN model

For obtaining the reasonable number of hidden neurons in the DBPNN model, the results of root-mean-square error (R_{MSE}) in Eq. (9) are listed in Table 1.

$$R_{\mathrm{MSE}} = \sqrt{\frac{1}{N}\sum_{l=1}^{N}(v(l) - \hat{v}(l))^2}, \quad (9)$$

where N is the number of data; $v(l)$ is the real value for the lth data; $\hat{v}(l)$ is the predictive value of the model for the lth data.

In Table 1, when the number of the DBPNN model is 10, the R_{MSE} is minimized, so the number of hidden neurons in the DBPNN model is finally determined to be 10.

Table 1 The comparison of the number of hidden layer neurons

Number of neurons	R_{MSE}
4	0.075 7
7	0.065 4
10	0.057 9
13	0.060 3
16	0.061 4

To identify the weights and thresholds of the DBPNN model, an input in Eq. (10) with the frequency and amplitude both being attenuated is used to excite the platform for training.

$$u(l) = 3.66\mathrm{e}^{-1.94\times10^{-3}l}\left[\sin\left(480\times\pi\times10^{-4}l\mathrm{e}^{-1.94\times10^{-3}l}\right)+1\right]. \quad (10)$$

On the other hand, to verify the generalization of the DBPNN model, another input signal in Eq. (11) is used to excite the platform for model verification.

$$u(l) = 3.56\mathrm{e}^{-1.74\times10^{-3}l}\left[\sin\left(400\times\pi\times10^{-4}l\mathrm{e}^{-1.8\times10^{-3}l}\right)+1\right]. \quad (11)$$

For comparison, a modified input rate-dependent Prandtl-Ishlinskii (MRPI) inverse model[21] with 10 backlash operators is applied to describe the inverse properties of the PEAs. The MRPI inverse model (abbreviated as the MRPI model) is as shown below:

$$v(l) = S[p](l) = h(p(l)) + \sum_{i=1}^{N_1} q_i H_{ri}[p](l), \quad (12)$$

$$h(p(l)) = b_1 p^3(l) + b_2 p(l), \quad (13)$$

$$H_{ri}[p](l) = \max\{p(l) - \alpha|\Delta p(l)| - r_i, \min\{p(l) + \beta|\Delta p(l)|, H_{ri}[p](l-1)\}\}, \quad (14)$$

where $\Delta p(l) = p(l) - p(l-1)$; r_i is initialized to $r_i = (i-1)/N_1 \cdot \|v_d(l)\|_\infty (i = 1, 2, \cdots, N_1)$, N_1 is number of the backlash operators; $\boldsymbol{b} = [b_1 \quad b_2]^{\mathrm{T}}$; $\boldsymbol{q} = [q_1 \quad \cdots \quad q_{N_1}]^{\mathrm{T}}$; α and β are unknown parameters.

The least squares algorithm is utilized to estimate parameters in the MRPI model, which are

$\boldsymbol{b} = [0.000\,3 \quad 0.687\,1]^{\mathrm{T}}$, $\alpha = 2.729\,5$, $\beta = 2.103\,4$ and

$\boldsymbol{q} = [-0.086\,8 \quad 0.052\,8 \quad -0.169\,4 \quad -0.011\,5 \quad -0.028\,5 \quad 0.023\,5 \quad -0.173\,6 \quad 0.057\,1 \quad 0.006\,9 \quad -0.097\,3]^{\mathrm{T}}$.

The compared results of the DBPNN model and MRPI model are shown in Fig. 11.

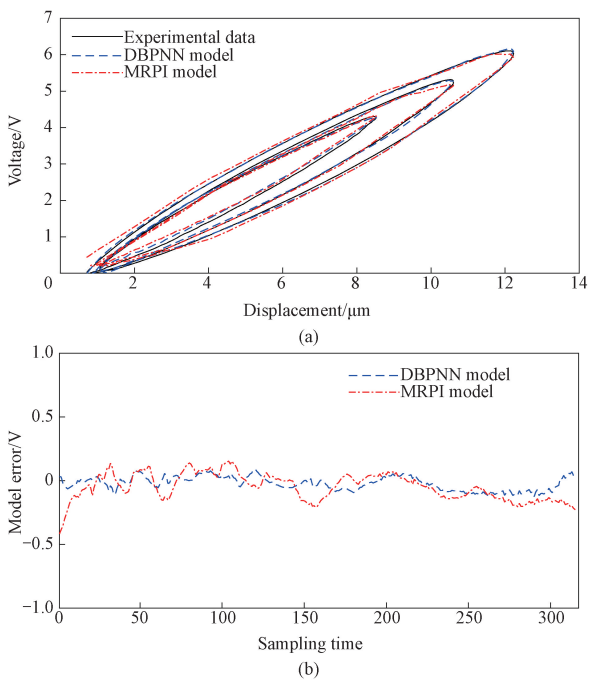

Fig. 11 Inverse model verification results: (a) voltage-displacement predictions obtained by the DBPNN and MRPI model; (b) model error of DBPNN and MRPI model

In Fig. 11, the solid line represents the real data; the dashed line represents the prediction result of the DBPNN model; the dotted line denotes the result of the MRPI model.

From Fig. 11(b), the model error of the DBPNN model is smaller, and the maximum relative error M_{RE} in Eq. (15) of the DBPNN model and MRPI model are about 2.05% and 6.82%, respectively.

$$M_{\mathrm{RE}} = \frac{\max|v(l) - \hat{v}(l)|}{\max(v) - \min(v)}. \quad (15)$$

3.2 Validation of the proposed hybrid controller

The proposed hybrid control scheme is applied in the PEAs to compensate for rate-dependent hysteresis. For comparison, a PID controller and a hybrid controller based on the MRPI model are both applied in the experimental platform, respectively.

In the experiment, the sampling frequency is 2 kHz, and the parameter in the filter is set to 0.9. $d_{\mathrm{r}}(l) = 5.9\mathrm{e}^{-1.6l\times10^{-4}} \times [\sin(10\pi\mathrm{e}^{5.6l\times10^{-4}} \times 2l \times 10^{-5}) + 1] + 1.8\mathrm{e}^{2l\times10^{-5}}$ is selected as a reference signal.

The parameters of the feedback PID controllers in the three different control schemes are shown in Table 2, and the tracking results are shown in Fig. 12.

Table 2 Parameters of PID controller under three different control strategies

Control strategy	Proportional gain K_p	Integral gain K_i	Derivative gain K_d
PID control	0.278	0.197	0.002 5
Hybrid control with MRPI model	0.115	0.165	0.002 0
Proposed hybrid control	0.318	0.323	0.002 0

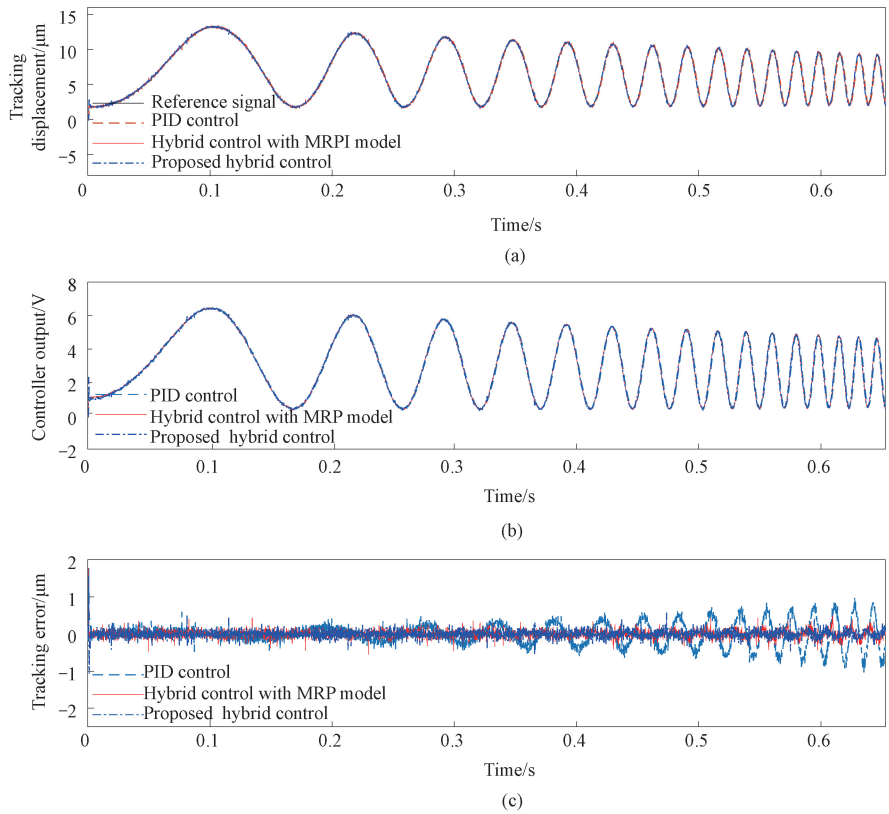

Fig. 12 Tracking results under dynamic sinusoidal signal

In Fig. 12, the dotted line represents the results of PID control, the solid line represents the results of the hybrid control with the MRPI model, and the dashed line represents the results of the proposed hybrid control. From Figs. 12(a) and 12(c), the proposed hybrid control can effectively compensate for the hysteresis when the frequency of input increases, and the tracking error is basically constant as the reference frequency increases, while the other two controllers have been influenced by input frequency. From Fig. 12(c), it is obvious that the proposed controller compared with the other two controllers has the best system performances, especially during the high frequency range. The maximum relative tracking errors of the three control methods are listed in Table 3, and from Table 3, the proposed hybrid control has the smallest control errors.

In addition, if the reference is a square wave signal, the experimental results are provided in Figs. 13 and 14. Figure 14 is the local amplification of Fig. 13. In Fig. 13, the dotted line denotes the results of PID control, the solid line represents the results of the hybrid control with the MRPI model, and the dashed line shows the results of the proposed hybrid control with the DBPNN model. In Figs. 13 and 14, at the rising edge of the square wave, the setting time t_s of the proposed hybrid control, the hybrid control with the MRPI model and the PID control are 7.5, 9.5 and 11 ms, respectively. Compared with the other two controllers, the proposed controller is the fastest, especially at the falling edge.

Table 3 Maximum relative error under three different control strategies

Control strategy	M_{RE}
PID control	0.076
Hybrid control with MRPI model	0.027
Proposed hybrid control	0.022

In a word, the experimental results demonstrate the feasibility and validation of the proposed control method.

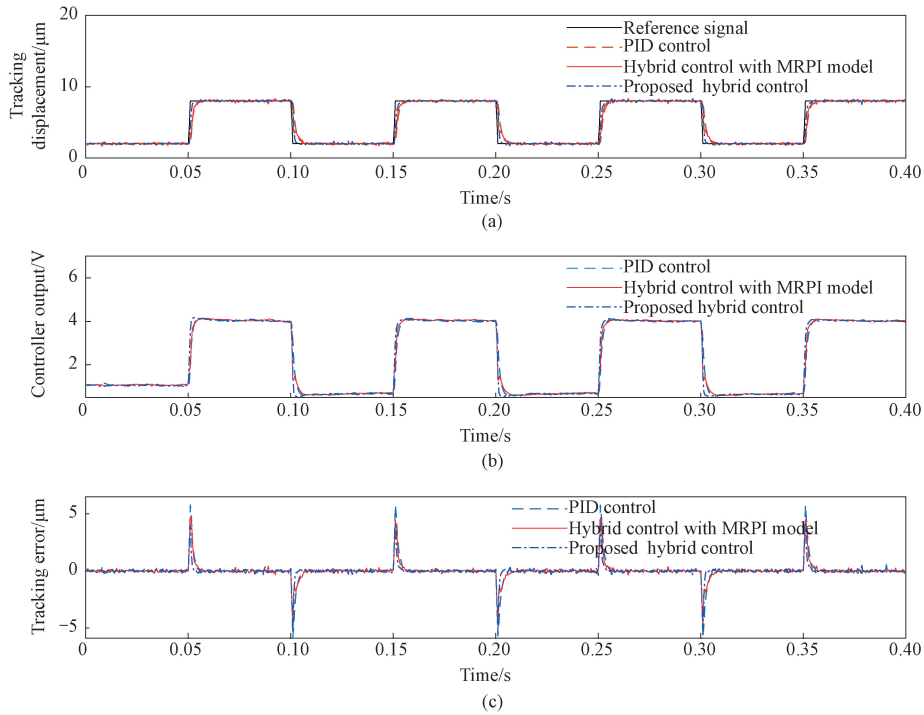

Fig. 13 Tracking results under square wave signal

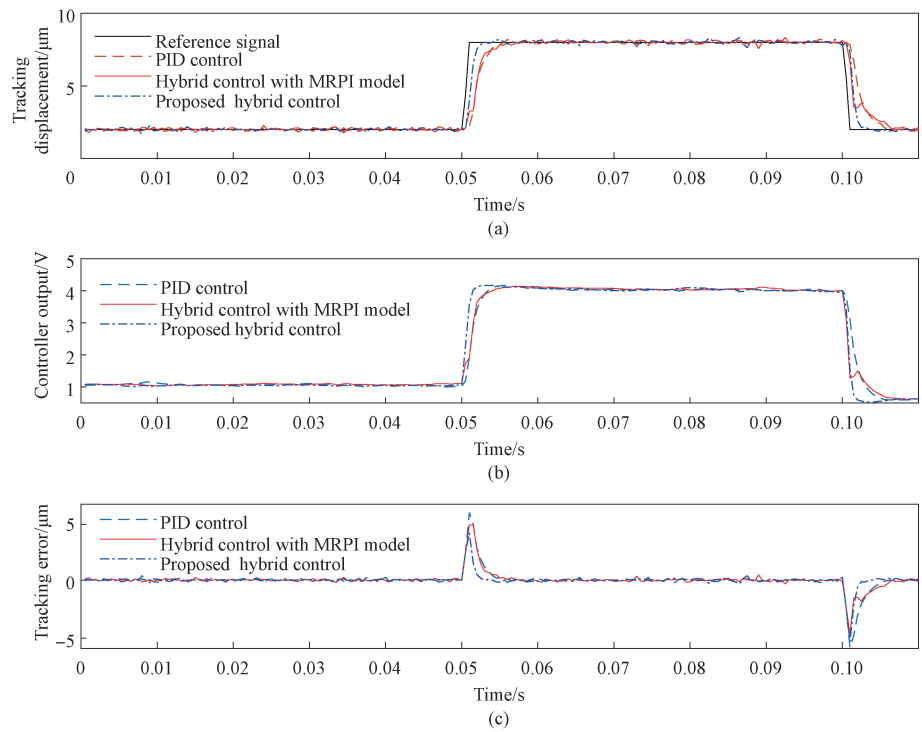

Fig. 14 Local amplification of Fig. 13

4 Conclusions

In this paper, a hybrid controller for the input rate-dependent hysteresis in PEAs is designed. The novelty of the proposed controller is mainly building the DBPNN model of rate-depended inverse hysteresis in the PEAs because the DBPNN model is a feedforward sub-controller in the designed hybrid controller. In the DBPNN model, two exponential terms exist in the RAIO, one characterizes the direction of the inverse hysteresis while the other extracts the frequency information of the input signal. In addition, the novel hybrid controller with the DBPNN model is designed.

Finally, the proposed hybrid controller with the DBPNN model, hybrid controller with MRPI model, and PID controller are all applied in the PEAs platform. The experimental results show that the proposed hybrid controller with the DBPNN model has better control performance.

References

[1] AKDOGAN E K, ALLAHVERDI M, SAFARI A. Piezoelectric composites for sensor and actuator applications[J]. *IEEE Transactions on Ultrasonics, Ferroelectrics, and Frequency Control*, 2005, 52(5): 746-775.

[2] BOUCHILLOUX P, CLAEYSSEN F, LE LETTY R. Amplified piezoelectric actuators: from aerospace to underwater applications[C]// SPIE Proceedings, Smart Structures and Materials 2004: Industrial and Commercial Applications of Smart Structures Technologies. Bellingham: SPIE, 2004, 5388: 143-154.

[3] HAUPT B J, PELLING A E, HORTON M A. Integrated confocal and scanning probe microscopy for biomedical research[J]. *The Scientific World Journal*, 2006, 6: 1609-1618.

[4] AGGOGERI F, AL-BENDER F, BRUNNER B, et al. Design of piezo-based AVC system for machine tool applications[J]. *Mechanical Systems and Signal Processing*, 2013, 36(1): 53-65.

[5] ZHANG Q, DONG Y C, PENG Y, et al. Asymmetric Bouc-Wen hysteresis modeling and inverse compensation for piezoelectric actuator via a genetic algorithm-based particle swarm optimization identification algorithm[J]. *Journal of Intelligent Material Systems and Structures*, 2019, 30(8): 1263-1275.

[6] LI Z, SHAN J J, GABBERT U. Inverse compensation of hysteresis using Krasnoselskii-Pokrovskii model[J]. *IEEE/ASME Transactions on Mechatronics*, 2018, 23(2): 966-971.

[7] RYBA Ł, VODA A, BESANÇON G. Experimental comparison of disturbance observer and inverse-based hysteresis compensation in 3D nanopositioning piezoactuation[J]. *Sensors and Actuators A: Physical*, 2015, 236: 190-205.

[8] RAAFAT S M, AKMELIAWATI R, ABDULLJABAAR I. Robust H_∞ controller for high precision positioning system, design, analysis, and implementation[J]. *Intelligent Control and Automation*, 2012, 3(3): 262-273.

[9] LIAW H C, SHIRINZADEH B, SMITH J. Enhanced sliding mode motion tracking control of piezoelectric actuators[J]. *Sensors and Actuators A: Physical*, 2007, 138(1): 194-202.

[10] PENG J Y, CHEN X B. Integrated PID-based sliding mode state estimation and control for piezoelectric actuators[J]. *IEEE/ASME Transactions on Mechatronics*, 2014, 19(1): 88-99.

[11] GU G Y, ZHU L M. Motion control of piezoceramic actuators with creep, hysteresis and vibration compensation[J]. *Sensors and Actuators A: Physical*, 2013, 197: 76-87.

[12] WANG G, CHEN G Q, BAI F Z. High-speed and precision control of a piezoelectric positioner with hysteresis, resonance and disturbance compensation[J]. *Microsystem Technologies*, 2016, 22(10): 2499-2509.

[13] CHEN Y S, WANG Z, WANG H, et al. Adaptive inverse of piezoelectric bimorph actuator with Prandtl-Ishlinskii model for wide-band tracking control[J]. *Journal of Physics: Conference Series*, 2020, 1633(1): 012025.

[14] TAO Y D, LI H X, ZHU L M. Rate-dependent hysteresis modeling and compensation of piezoelectric actuators using Gaussian process[J]. *Sensors and Actuators A: Physical*, 2019, 295: 357-365.

[15] MAO X F, WANG Y J, LIU X D, et al. A hybrid feedforward-feedback hysteresis compensator in piezoelectric actuators based on least-squares support vector machine[J]. *IEEE Transactions on Industrial Electronics*, 2018, 65(7): 5704-5711.

[16] MENG D, XIA P Q, LANG K, et al. Neural network based hysteresis compensation of piezoelectric stack actuator driven active control of helicopter vibration[J]. *Sensors and Actuators A: Physical*, 2020, 302: 111809.

[17] GORBET R B. Control of hysteretic systems with preisach representations[D]. Ontario: University of Waterloo, 1997.

[18] DONG R L, TAN Y H, CHEN H, et al. A neural networks based model for rate-dependent hysteresis for piezoceramic actuators[J]. *Sensors and Actuators A: Physical*, 2008, 143(2): 370-376.

[19] MARQUARDT D W. An algorithm for least-squares estimation of nonlinear parameters[J]. *Journal of the Society for Industrial and Applied Mathematics*, 1963, 11(2): 431-441.

[20] FU X G, LI S H, FAIRBANK M, et al. Training recurrent neural networks with the levenberg-marquardt algorithm for optimal control of a grid-connected converter[J]. *IEEE Transactions on Neural Networks and Learning Systems*, 2015, 26(9): 1900-1912.

[21] YANG M J, LI C X, GU G Y, et al. Modeling and compensating the dynamic hysteresis of piezoelectric actuators via a modified rate-dependent Prandtl-Ishlinskii model[J]. *Smart Materials and Structures*, 2015, 24(12): 125006.

Appendix A Proof of Lemma 1

Case 1: The input is not at the extreme point.

According to Eq. (3), it is clear that the conclusion is true.

Case 2: The input is at the extreme point, such as at a local maximum point p_{e2} in Figs. 6 and 7. Based on Eq. (3), $g(p_{e2}, 0)$ is described as

$$g(p_{e2},0) = e^{d_1(p_{e2}-p_{e1})} - e^{d_2|0|}(p_{e2}-p_{e1}) + g(p_{e1},0) - 1, \tag{A1}$$

and

$$g(p_{e2}^-, 0^+) = \lim_{\substack{p(l)\to p_{e2}^- \\ \Delta p(l)\to 0^+}} g(p(l), \Delta p(l)) = e^{d_1(p_{e2}^- - p_{e1})} - e^{d_2|0^+|}(p_{e2}^- - p_{e1}) + g(p_{e1}, 0) - 1. \tag{A2}$$

Combining Eq. (A1) and Eq. (A2) to remove -1 in Eq. (A2) results in

$$g(p_{e2}^-, 0^+) = e^{d_1(p_{e2}^- - p_{e1})} - e^{d_2|0^+|}(p_{e2}^- - p_{e1}) + g(p_{e2}, 0) - e^{d_1(p_{e2}-p_{e1})} + e^{d_2|0|}(p_{e2}-p_{e1}). \tag{A3}$$

As $\lim_{p\to p_{e2}^-}[p - p_{e2}] \to 0^-$, it has $p_{e2}^- \to p_{e2}$. So that

$$g(p_{e2}^-, 0^+) = g(p_{e2}, 0). \tag{A4}$$

Similarly,

$$g(p_{e2}^+,0^-) = \lim_{\substack{p(l)\to p_{e2}^+ \\ \Delta p(l)\to 0^-}} g(p(l), \Delta p(l)) = -e^{-d_1(p_{e2}^+ - p_{e2})} - e^{d_2|0^-|}(p_{e2}^+ - p_{e2}) + g(p_{e2},0) + 1. \tag{A5}$$

As $\lim_{p\to p_{e2}^+}[p - p_{e2}] \to 0^+$, it has $p_{e2}^+ \to p_{e2}$. So that

$$g(p_{e2}^+, 0^-) = g(p_{e2}, 0). \tag{A6}$$

So, it results in

$$g(p_{e2}^+, 0^-) = g(p_{e2}^-, 0^+) = g(p_{e2}, 0). \tag{A7}$$

It can be concluded that $g(p(l), \Delta p(l))$ is continuous at the local maximum point. Similarly, it can be derived that $g(p(l), \Delta p(l))$ also is continuous at the local minimum point. In summary, it is proved that $g(p(l), \Delta p(l))$ is a continuous function of the input $p(l)$.

Appendix B Proof of Lemma 2

As shown in Figs. 6 and 7, for $p(l')$ in the ascending curve of the input signal, Eq. (3) can be rewritten as

$$g(p(l'), \Delta p(l')) = e^{d_1(p(l')-p_{e1})} - e^{d_2|\Delta p(l')|}(p(l') - p_{e1}) + g(p_{e1}, 0) - 1. \tag{B1}$$

And for $p(l'')$ in the descending curve of the input signal, Eq. (3) can be rewritten as

$$g(p(l''), \Delta p(l'')) = -e^{-d_1(p(l'')-p_{e2})} - e^{d_2|\Delta p(l'')|}(p(l'') - p_{e2}) + g(p_{e2}, 0) + 1. \tag{B2}$$

Apply Eq. (B2) to get $g(p_{e2}, 0)$, and it can be obtained

$$g(p_{e2}, 0) = e^{d_1(p_{e2}-p_{e1})} - e^{d_2|0|}(p_{e2} - p_{e1}) + g(p_{e1}, 0) - 1. \tag{B3}$$

Eq. (B1) minus Eq. (B2), and substitute Eq. (B3) into Eq. (B2), and it gets

$$\begin{aligned} g(p(l'), \Delta p(l')) - g(p(l''), \Delta p(l'')) = {} & e^{d_1(p(l')-p_{e1})} - e^{d_2|\Delta p(l')|}(p(l') - p_{e1}) + e^{d_1(p_{e2}-p(l''))} \\ & + e^{d_2|\Delta p(l'')|}(p(l'') - p_{e2}) - e^{d_1(p_{e2}-p_{e1})} + (p_{e2} - p_{e1}) - 1 \end{aligned}. \tag{B4}$$

For $p \neq p_{e1}$, $p \neq p_{e2}$, let $e^{d_2|\Delta p(l')|} = a$ $(a > 1)$, $e^{d_2|\Delta p(l'')|} = b$ $(b > 1)$, and Eq. (B4) can be rewritten as

$$F(p) = e^{d_1(p-p_{e1})} - a(p - p_{e1}) + e^{d_1(p_{e2}-p)} + b(p - p_{e2}) - e^{d_1(p_{e2}-p_{e1})} + (p_{e2} - p_{e1}) - 1. \tag{B5}$$

In fact, $F(p) = g(p(l'), \Delta p(l')) - g(p(l''), \Delta p(l''))$.

Separate Eq. (B5) into two terms, then

$$F_1(p) = e^{d_1(p-p_{e1})} + e^{d_1(p_{e2}-p)} - e^{d_1(p_{e2}-p_{e1})} - 1, \tag{B6}$$

$$F_2(p) = -a(p - p_{e1}) - b(p_{e2} - p) + (p_{e2} - p_{e1}), \tag{B7}$$

where $F(p) = F_1(p) + F_2(p)$.

For $p_{e2} \neq p_{e1}$ and $p_{e1} < p < p_{e2}$, combining the monotonicity of $F_1(p)$ in Eq. (B6), it obtains $F_1(p) < 0$. (B8)

Additionally, owing to $a > 1$ and $b > 1$, for Eq. (B7), we can get

$$F_2(p) = -a(p - p_{e1}) - b(p_{e2} - p) + (p_{e2} - p_{e1}) < -(p - p_{e1}) - (p_{e2} - p) + (p_{e2} - p_{e1}) = 0. \tag{B9}$$

Then

$$F(p) < 0. \tag{B10}$$

Namely,

$$g(p(l'),\ \Delta p(l'))\neq g(p(l''),\ \Delta p(l''))\ . \tag{B11}$$

Lemma 2 is proved.

Appendix C Proof of Theorem 1

Firstly, we prove that E is a one-to-one mapping divided into two cases.

Case 1: Supposing that $p(l')$ and $p(l'')$ are not extreme points.

Based on Eq. (B10), it can derive that

$$E(p(l'),\ g(p(l'),\ \Delta p(l')))\neq E(p(l''),\ g(p(l''),\ \Delta p(l'')))\ . \tag{C1}$$

Case 2: Supposing that $p(l')$ and $p(l'')$ are extreme points.

Based on Eq. (B5), $a=b=1$. Hence, $F(p)=0$, then

$$g(p(l'),\ \Delta p(l'))=g(p(l''),\ \Delta p(l''))\ . \tag{C2}$$

It leads to

$$E(p(l'),\ g(p(l'),\ \Delta p(l')))=E(p(l''),\ g(p(l''),\ \Delta p(l'')))\ . \tag{C3}$$

Secondly, we prove that the mapping E is continuous.

According to Lemma 1, if $p(l_1)-p(l_2)\to 0$ for different l_1 and l_2, then we can get

$$g(p(l_1),\ \Delta p(l_1))-g(p(l_2),\ \Delta p(l_2))\to 0\ . \tag{C4}$$

Neural networks can continuously approximate nonlinear functions with arbitrary precision, thus

$$\varphi(p(l_1))-\varphi(p(l_2))\to 0\ . \tag{C5}$$

In summary, $E:\mathbf{R}^2\to\mathbf{R}$ is a continuous one-to-one mapping. Hence, the output of the dynamic hysteresis model can be uniquely determined by any one of the input values.

压电陶瓷致动器输入速率相关迟滞的混合补偿方案

董瑞丽[1*]，谭永红[2*]，侯佳佳[1]，郑榜生[1]

1. 东华大学 信息科学与技术学院，上海 201620

2. 上海师范大学 机械与电子工程学院，上海 200234

摘　要：提出了一种关于压电陶瓷致动器的混合补偿方案。在混合补偿方案中，对压电陶瓷致动器的输入速率相关迟滞特性进行了补偿。前馈控制器是一种新型的输入速率相关的神经网络迟滞逆模型，而反馈控制器为比例−积分−微分（proportion integration differentiation，PID）控制器。在所提出的逆模型中，输入速率相关辅助逆算子（rate-dependent auxiliary inverse operator，RAIO）和迟滞的输出构造了逆模型的扩展输入空间（expanded input space，EIS），将多值映射的迟滞逆映射转换为单值映射，并在理论上分析了所提 RAIO 的消去、输入速率相关特性和连续性。基于 EIS 方法，建立了迟滞的神经网络逆模型，即动态反向传播神经网络（dynamic back propagation neural network，DBPNN）模型。此外，还设计了针对压电陶瓷致动器的混合补偿方案来补偿迟滞。最后，将所提方法、常规 PID 控制器和含改进的输入速率相关的 Prandtl-Ishlinskii 逆模型的混合控制器应用于实验。实验结果表明，所提方法在系统性能上具有明显的优势。

关键词：混合控制；输入速率相关的迟滞；逆模型；神经网络；压电陶瓷致动器